ELSEVIER

Theoretical and Applied Fracture Mechanics 37 (2001) 311–334

theoretical and applied fracture mechanics

www.elsevier.com/locate/tafmec

Movable cellular automata method for simulating materials with mesostructure

S.G. Psakhie [a,*], Y. Horie [b], G.P. Ostermeyer [c], S.Yu. Korostelev [a], A.Yu. Smolin [a], E.V. Shilko [a], A.I. Dmitriev [a], S. Blatnik [e], M. Špegel [d], S. Zavšek [f]

[a] *Institute of Strength Physics and Materials Science, Russian Academy of Sciences, pr. Academicheskii 2/1, Tomsk 634021, Russia*
[b] *Los Alamos National Laboratory, MS D413, X-MH, Los Alamos, NM 87545, USA*
[c] *University of Braunschweig, Institute of Engineering Mechanics, Schleinitzstrasse 20, D-38106 Braunschweig, Germany*
[d] *Jozef Stefan Institute, Jamova 39, SI-1000 Ljubljana, Slovenia*
[e] *IPAK, Koroška 18, SI-3320 Velenje, Slovenia*
[f] *Velenje Coal Mine, Partizanska 78, SI-3320, Velenje, Slovenia*

Abstract

Mathematical formalism and applications of the movable cellular automata (MCA) method are presented for solving problems of physical mesomechanics. Since the MCA is a discrete approach, it has advantages over that of the finite element method (FEM). Simulation results agree closely with the experimental data. The MCA approach cab solves mechanical engineering problems ranging from those in material science to those in structures and constructions. Computer simulation using MCA can also provide useful information in situations where direct measurements are not possible. © 2001 Published by Elsevier Science Ltd.

1. Introduction

Mechanics is the science that treats motion. A Material to be described can be represented as a continuum or multitude of interacting particles. These approaches were suggested by Cauchy and Navier, in the early 19th century. The continuum approach prevailed for a long period of time.

The development and elaboration of numerical methods were an important stage in the development of mechanics. It was associated with the advent of computer. Computational mechanics is considered to be an independent part of mechanics that supplements theoretical and experimental investigations; it is often referred to as computer experiments.

Digitization has also improved accuracy of numerical solutions, particularly for solving the equations of continuum mechanics. Advances in computational mechanics cannot be overemphasized for its application to virtual testing and design. Discrete computational mechanics has been developed as Molecular Dynamics problems at the atomic level. However, the potentials of the discrete approach are by no means fully developed.

The last 15–20 years have been marked by works where the particle method was used to de-

* Corresponding author. Tel.: +7-382-2-258881; fax: +7-382-2-259576.
E-mail addresses: sp@ms.tsc.ru, psakhie@yahoo.com (S.G. Psakhie).

0167-8442/01/$ - see front matter © 2001 Published by Elsevier Science Ltd.
PII: S0167-8442(01)00079-9

scribe different media including granular and loose materials. These works can be found in [1–11]. In addition to the conventional Newton–Euler equations of motion, moment equations are also used. Particle interaction (including atoms) considers the nearest neighbor with a time step integration of equations of motion [12,13]. While the adiabatic assumption has made those analyses meso- and macrolevels involve certain artificial expedients when integrating equations of motion. Thus, the models based on the conventional Newton–Euler addresses point masses, even though they include the moment equations. To overcome this contradiction, the method of movable cellular automata (MCA) [14–16] was developed by the authors in the framework of joint projects.

2. MCA method

2.1. Basic approach

Consider a system to be simulated by an ensemble of interacting automata (elements) of finite size [16]. The concept of this method is based on the introduction of a new type of states, viz., the state of a pair of automata, into that of classical cellular automata. This has made possible a space variable that serves as a parameter of switching. The overlapping of a pair of automata was chosen as

$$h^{ij} = r^{ij} - r_0^{ij}, \tag{1}$$

which is exhibited in Fig. 1(a). The distance r^{ij} between the centers of neighboring automata is shown in Fig. 1(b) with d^i being the automata size.

For the simplest case, two states of pairs prevail:

$$\text{Linked state:} \quad h^{ij} < h^{ij}_{\max}, \tag{2}$$

$$\text{Unlinked state:} \quad h^{ij} > h^{ij}_{\max}. \tag{3}$$

The linked state is indicative of chemical bonds between elements and the unlinked state corresponds to the situation that there is no chemical bond between automata. Note that h^{ij} and r^{ij} are length parameters. They are capable of changing their positions in space and, consequently, changing the spatial arrangement of the entire system. The change in state of the automata pairs is governed by relative displacements of the automata pair. It follows from Eqs. (2) and (3) that the given medium constituted by such pairs can be considered as a bistable medium.

Consider a pair of automata ij. The state of this pair of automata is uniquely determined by two types of fields $h^{\alpha\beta}(t)$. The first is associated with the state of the pair itself ij–$h^{ij}(t)$ and the second is associated with the states of its neighboring pairs $\{ik\}$–h^{ik} and $\{jl\}$–h^{jl}. It is worthy of note that these fields define local deformations (deformation of elements of the medium) and, consequently, the distribution and fluxes of elastic energy in the simulated medium.

The time derivative $h^{ij}(t)$ can be determined following the Viner–Rothenblute model [17]. The active bistable medium under study can be described by the equation

$$\frac{\Delta h^{ij}}{\Delta t} = f(h^{ij}) + \sum_{k\neq j} C(ij,ik) I(h^{ik}) + \sum_{l\neq i} C(ij,jl) I(h^{jl}), \tag{4}$$

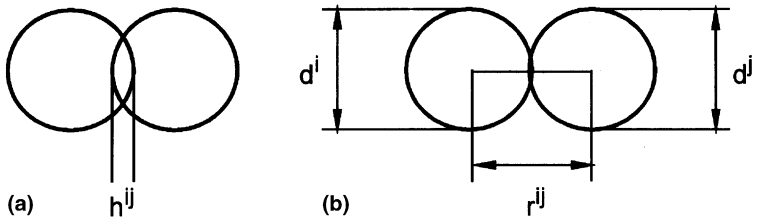

Fig. 1. Pair of automata: (a) overlapping state, (b) contact state.

where the function $f(h^{ij})$ is indicative of the relative velocity of automata (V^{ij}) and $C(ij, ik(jl))$ the coefficient associated with the transfer of the parameter h from the pair ik (or jl) to the pair ij with $I(h^{ik(jl)})$ being an explicit function of $h^{ik(jl)}$. Here $h^{ik(jl)}$ defines the redistribution of the parameters h^{ik} and h^{jl} between the pairs ij, ik, and jl. These parameters are shown in Fig. 2.

Within the linear approximation, the function $I(h^{ik(jl)})$ can be written as

$$I(h^{ik(jl)}) = \psi(\alpha_{ij,ik(jl)})V_n^{i(k)(j(l))}. \tag{5}$$

In general, the multiplier $\psi(\alpha_{ij,ik(jl)})$ is a combination of trigonometrical functions and is defined by mutual arrangements of the automata ij, ik, and jl. Note that $\alpha_{ij,ik(jl)}$ is a set of values of the corresponding angles defined by the relative arrangement.

The change in the overlapping parameter h^{ij} for the pair ij is defined by the following factors:

- relative velocity between the elements i and j (V^{ij});
- change in the overlaps (Δh^{ij}) of the ith automaton and its neighbors;
- change in the overlaps (Δh^{jl}) of the jth automaton and its neighbors.

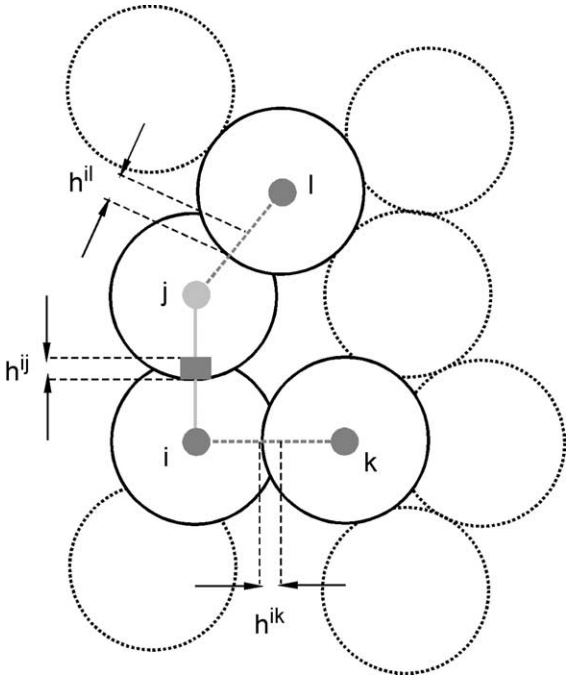

Fig. 2. Overlapping parameters for the pairs ij, ik, and jl.

2.2. Motion of MCA

It follows from Eq. (1) that the system consisting of movable cellular automata shall be described by the translational equations of motion given by

$$\frac{\mathrm{d}^2h^{ij}}{\mathrm{d}t^2} = \left(\frac{1}{m^i} + \frac{1}{m^j}\right)p^{ij} + \sum_{k\neq j} C(ij, ik)\psi(\alpha_{ij,ik})\frac{1}{m^i}p^{ik} + \sum_{l\neq i} C(ij, jl)\psi(\alpha_{ij,jl})\frac{1}{m^j}p^{jl}. \tag{6}$$

To obtain Eq. (6), the term $(\mathrm{d}/\mathrm{d}t)V^{i(j)k(l)}$ was represented as $(1/m^i)p^{i(j)k(l)}$, where $p^{i(j)k(l)}$ is the force of inter-element interaction. It is defined by the function of the inter-automata response. The coefficient $C(ij, ik(jl))$, as stated in Eq. (4), is associated with the transfer of the parameter h from the pair ik (or jl) to the pair ij. The term $\psi(\alpha_{ij,ik})$ in Eq. (5) is determined by the Poisson ratio and is related to the mutual arrangement of the pairs of elements ij and ik.

The equations of motion for rotation can be written as

$$\frac{\mathrm{d}^2\theta^{ij}}{\mathrm{d}t^2} = \left(\frac{q^{ij}}{J^i} + \frac{q^{ji}}{J^j}\right)\tau^{ij} + \sum_{k\neq j} S(ij, ik)\frac{q^{ik}}{J^i}\tau^{ik} + \sum_{l\neq i} S(ij, jl)\frac{q^{jl}}{J^j}\tau^{jl}. \tag{7}$$

Here, θ^{ij} is the angle of the relative rotation of elements (switching parameter) similar to h^{ij}; q^{ij} the distance from the center of the automaton i to the point of contact with the automaton j (moment arm); τ^{ij} the tangential interaction of pairs; and $S(ij, ik(jl))$ the coefficients associated with the transfer of the parameter θ from the pair ik (or jl) to the pair ij. If $C(ij, ik(jl)) = 1$ and $S(ij, ik(jl)) = 1$, Eqs. (6) and (7) are completely equivalent to the Newton–Euler equations of motion for many-particle interaction.

As noted above, the term $C(ij, ik(jl))$ determines the transfer of the parameter h from the pair ik (or jl) to the pair ij. The term "elastic information" implies information for relative elastic displacements of elements transferred to elastic fields. Hence, equations of motion or Eqs. (6) and (7) make it possible to allow for "delays" $\delta t^{ij(ik)}$ and $\delta t^{ij(il)}$. This affects the overlapping parameter for the pairs $\{ik\}$ and $\{jl\}$ on the interaction of the pair of elements ij (Fig. 2). The time lag is defined by the automata sizes, longitudinal and transverse sound velocities, and mutual arrangement of the pairs ij and ik (or jl). It is obvious that the effects associated with generation and propagation of shock waves require particular attention.

2.3. Volumetric changes

For the method of embedded particles, Eqs. (6)and (7) can be written as

$$m^i \frac{\mathrm{d}^2 \mathbf{R}^i}{\mathrm{d}t^2} = \mathbf{F}^i_\Omega + \sum_j \mathbf{F}^{ii}, \quad \widehat{j}^{\,i} \frac{\mathrm{d}^2 \vec{\theta}^i}{\mathrm{d}t^2} = \sum_j \mathbf{K}^{ij}, \tag{8}$$

where $\mathbf{F}^i_\Omega$ is the volume-dependent force acting on the automaton i caused by the action of pressure from neighboring automata, $\mathbf{F}^i = \mathbf{p}^{ij} + \boldsymbol{\tau}^{ij}$. Here $\mathbf{p}^{ij}$ is the central component of the pair interaction force and $\boldsymbol{\tau}^{ij}$ the tangential component of this force. $\mathbf{K}^{ij} = q^{ij}(\mathbf{n}^{ij} \times \boldsymbol{\tau}^{ij})$ is the unit vector $\mathbf{n}^{ij}$ defined as $\mathbf{n}^{ij} = (\mathbf{R}^j - \mathbf{R}^i)/(q^{ij} + q^{ji})$.

The volume-dependent force $\mathbf{F}^i_\Omega$ acting on the automaton i due to the action of pressure from surroundings can be accounted for similar to the embedded atom method (EAM) known from molecular dynamics [18]:

$$\mathbf{F}^{\mathrm{i}}_\Omega = \sum_j P^j S^{ij} \mathbf{n}^{ij}. \tag{9}$$

The index j ($j = 1, \ldots, N^i$) refers to automata in the linked state or the contact state with automaton i. It should be noted that P^j is the pressure of the jth neighbor; S^{ij} the area of contact of the automaton i with the automaton j; and $\mathbf{n}^{ij}$ the unit vector of the normal to the contact area. Here $\mathbf{n}^{ij}$ is directed towards the neighbor j. The automaton pressure is determined by the change in the automation volume. In the simplest (linear) case this dependence takes the form

$$P^j = K^j \frac{\Omega^j - \Omega^j_0}{\Omega^j_0}, \tag{10}$$

where Ω^j_0 is the initial (equilibrium) automaton volume; Ω^j the current automaton volume; and K^j the bulk modulus. The simplest approximation corresponds to the change in the automaton volume for a time Δt. It can be determined from the corresponding changes in the distances Δq^{jk} from the center of this automaton to the points of its contact with neighbors, i.e.,

$$\Delta\Omega^j = \Omega^j \sum_{k=0}^{N^j} \Delta q^{jk} \Bigg/ \left(\sum_{k=0}^{N^j} q^{jk} \Bigg/ N^j \right), \tag{11}$$

where N^j is the number of neighbors of the automaton j.

2.4. Response function

For each automation, the relative deformation ε^{ij} is introduced. Refer to Fig. 3. The parameter q^{ij} is the distance between the mass center of the automaton i and the point of its contact with the automaton j.

It is possible to set aside four basic types of the response function (Fig. 4). For the simplest case, the inter-automata interaction is assumed elastic and linear. Hence, the response function can be treated as a linear function of the overlapping parameter, Fig. 4(a). The switching of the automata pair from the linked to unlinked state occurs when their overlapping reaches a value corresponding to σ_c.

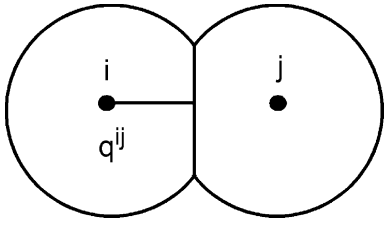

Fig. 3. Scheme for calculating relative deformation of automata.

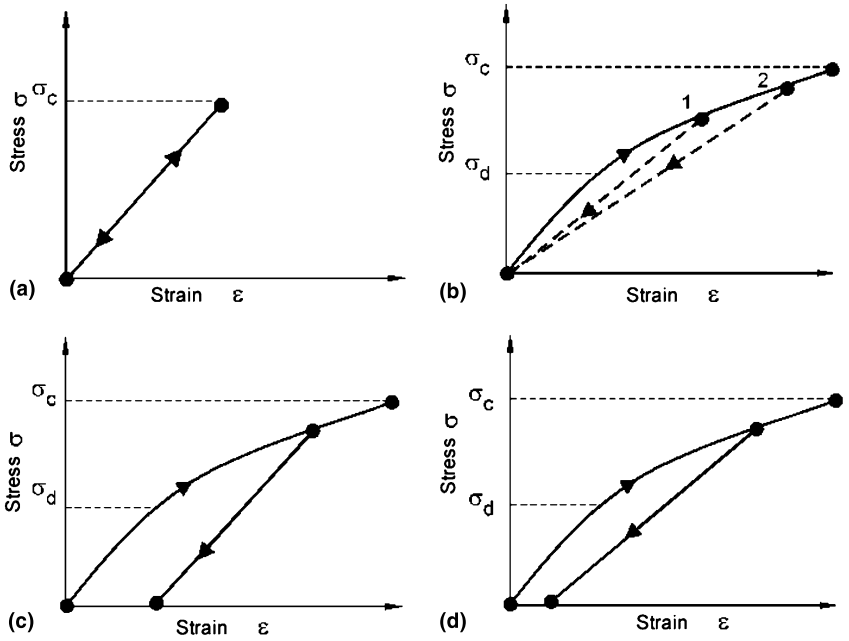

Fig. 4. Different types of material response: (a) linear, (b) concrete like material, (c) plastic deformation, (d) plastic flow and degradation.

To account for damage at a scale level lower than the automation size, the linear response function should be modified. Fig. 4(b) represents the response. The effective Young's modulus decreases due to degradation corresponding to a given load higher than σ_d. This degradation is caused by damage generation. Note that the linear response is observed in the range of loading $\langle 0 - \sigma_d \rangle$ whereas in the range of $\langle \sigma_d - \sigma_c \rangle$ damages are generated within automata. The response function is nonlinear in character. Unloading is defined by a new Young's modulus represented by dotted lines in Fig. 4(b). For each point of the response, see points 1 and 2 in the range of $\langle \sigma_d - \sigma_c \rangle$, the Young's moduli are different. The response in Fig. 4(a) and (b) can be used for simulating the process of fracture of brittle materials such as ceramics, concrete, etc., and constructions designed based on such materials. The responses for irreversible materials behavior are shown in Fig. 4(c) and (d). Presented in Fig. 4(c) is plastic deformation while Fig. 4(d) represents a combination of plastic flow and material degradation. The response of irreversible behavior, say plastic deformation, requires an intimate knowledge of the mechanisms of plastic flow initiation and evolution [19,20].

Nevertheless, the MCA method could be applied to simulate the behavior of specimens and structures provided that detail information is available on the material behavior in the region of plastic flow. The MCA method could simulate the processes of elastoplastic deformation and material degradation at the meso- and microlevels selecting appropriate response functions for the movable automata [14–16,21].

2.5. Surface interaction

When simulating surface friction using the particle approach, a serious problem arises with reference to the correct setting of surface structures and interaction. Modeling the solid as a set of particles, all surfaces are assumed to be artificially rough and regular. It can be seen from Fig. 5 that the roughness characteristics are associated with the element size.

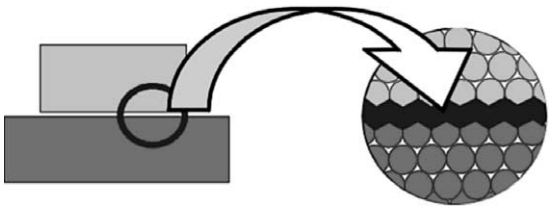

Fig. 5. Artificial structure of surfaces for two contacting solids simulated as a set of particles.

In general, three levels of a real surface will be considered. They are referred to as the macrolevel (solid as whole), microlevel (voids, small cracks, etc.) and mesolevel (intermediate properties of the two just mentioned) [22,23].

Two ways of simulating a contact surface are:

- The automata sizes are specified to be so small that they describe (topologically) the real surface roughness. This allows direct investigation of the processes at all three scale levels mentioned. In this case the surface roughness, material inhomogeneity, and other structural defects (such as damages, cracks, etc.) can be introduced in an explicit form through the topology of a surface layer.
- The automata sizes are specified to be so large that they consider the contacting surface as a plane with roughness preset directly at a lower level. Such an approximation makes it possible to cover the macro- and mesolevels. The interaction of two contacting surfaces can be described by introducing friction forces, which depend on the microparameters of the surface.

Even with the advent of modern high-power computers, the first approach is limited to examination of small areas of contacting surfaces, Fig. 6(a) because a great number of elements is required to describe a real surface. On the other hand, such an approximation can be used to study the mechanisms of very intricate processes occurring in surface layers of materials, e.g., damage generation and accumulation, crack propagation, changes in the surface profile, structure, and composition of materials near the surface. The results can be useful for understanding the causes and tendencies of phenomena at the mesolevel. However, the results for an element may not be sufficient to simulate the interaction of two contacting surfaces at the macrolevel.

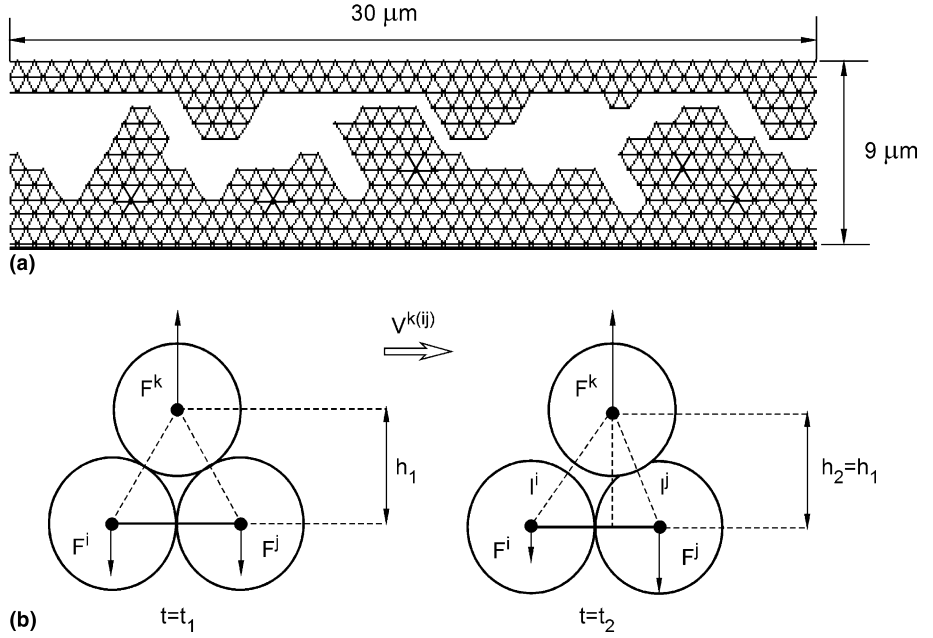

Fig. 6. Description of contacting surfaces: (a) direct setting of micro-roughness, (b) indirect setting at the meso-level.

The second approach considers the contacting surfaces as a set of segments for the two-dimensional (2D) case and surface elements for the 3D case. The 3D case is shown schematically in Fig. 6(b). The automata i and j correspond to the lower surface and the automaton k corresponds to the upper surface. The pair i–j is considered as a segment interacting with the automaton k.

Two types of "segment–element" interaction will be used. They correspond to the normal potential interaction and tangential friction force.

The normal interaction is defined by the height h between the element k and segments i–j. The normal force is applied to each automation of the triangle k–i–j according to

- $F^{k(ij)}$ is the force acting on the automaton k from the side of the segment i–j:

$$F^{k(ij)}\left(h_n^{k(ij)}\right) = E\left(\frac{h_n^{k(ij)} - h_0^{k(ij)}}{h_0^{k(ij)}}\right). \tag{12}$$

- $F^{(ij)k}$ is the force acting from the side of the automaton k on the element j as a part of the segment i–j:

$$F^{(ji)k}\left(h_n^{k(ij)}\right) = \frac{El^j}{r^{ij}}\left(\frac{h_n^{k(ij)} - h_0^{k(ij)}}{h_0^{k(ij)}}\right). \tag{13}$$

- $F^{(ji)k}$ is the force acting from the side of the automaton k on the element j as a part of the segment i–j:

$$F^{(ji)k}\left(h_n^{k(ij)}\right) = \frac{El^i}{r^{ij}}\left(\frac{h_n^{k(ij)} - h_0^{k(ij)}}{h_0^{k(ij)}}\right). \tag{14}$$

The equilibrium distance (height) h_0 for the "segment–element" interaction is defined as $h_0 = \sqrt{3}R$, where R is the automaton radius. It can be seen that $F^{k(ij)} = F^{(ij)k} + F^{(ji)k}$.

The tangential interaction of two contacting surfaces is described by the dissipative friction force. Mesofragments of the contacting surfaces are considered as plane. Hence, the tangential interaction "segment–element" can be written. Analogues to Eqs. (12)–(14), it can be shown that

$$F_{\mathrm{R}}^{k(ij)}(V_\tau) = F_{\mathrm{R}}, \tag{15}$$

$$F_{\mathrm{R}}^{(ij)k}(V_\tau) = \frac{F_{\mathrm{R}}\, l^j}{r^{ij}}, \tag{16}$$

$$F_{\mathrm{R}}^{(ji)k}(V_\tau) = \frac{F_{\mathrm{R}}\, l^j}{r^{ij}}, \tag{17}$$

where F_{R} is the local friction force. The resistance to the relative tangential displacement is defined by the surface roughness characteristics at the microlevel. In the present work the general expression for the local force of friction at the mesolevel has the form

$$F_{\mathrm{R}} = \mu_0 V_\tau + f(\mu_1, K_\mu, \sigma_{\mathrm{N}}, \sigma_0, V_\tau). \tag{18}$$

The first part in Eq. (18) represents viscous friction and the second part describes friction resulting from local interaction of contacting surfaces. Here, V_τ is the tangential velocity; μ_0 the viscous friction coefficient; f is some function; μ_1 the friction coefficient for dry surfaces; σ_{N} the normal compressive stresses; σ_0 the elastic limit; and K_μ a special variable describing the local resistance due to the relative tangential displacement of contacting surfaces at the microlevel. In general, the parameters $\mu_0, \mu_1, \sigma_{\mathrm{N}}$, and K_μ are complex functions of different microscale factors such as the local profile of the contact surface ξ, history of interaction L, tangential velocity V_τ, local compressive normal stresses $\sigma_{\mathrm{N}}^{\mathrm{local}}$, local temperature T^{local}, etc. The variable K_μ is also a function of the average contact area S. Different forms of the dependence of Eq. (18) on the variables have been used to study the friction effects at the meso- and macrolevels [24,25]. In practice, use is often made of the macrocharacteristics such as the coefficient of friction of two surfaces:

$$\mu_{\mathrm{dr}} = \frac{F_{\mathrm{dr}}}{F_{\mathrm{N}}}. \tag{19}$$

In Eq. (19), F_{dr} is the resistance of the contacting solids to relative tangential movement and F_{N} is the applied normal force. It is possible to obtain different forms for μ_{dr} with reference to friction time and frequency, path covered, initial temperature, and surface state and other frictional characteristics at the mesoscale level.

2.6. Surface microroughness

The variable K_μ, describes the microroughness. It is a real dependence $K_\mu(\xi)$ as shown in Fig. 7(a)

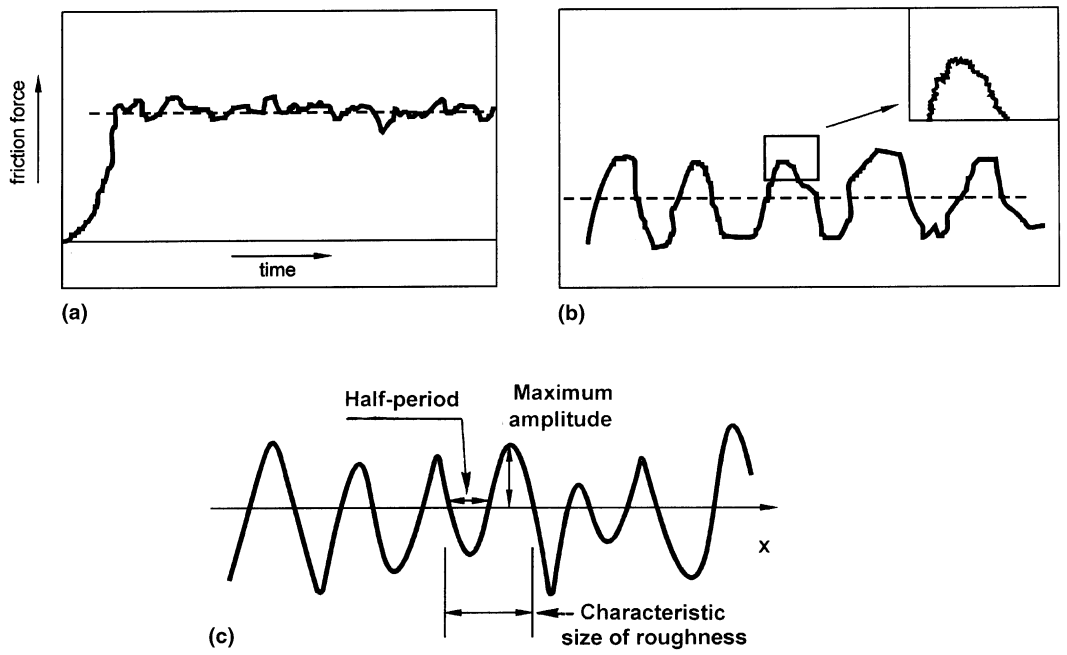

Fig. 7. Surfaces roughness characteristics: (a) experiment, (b) MCA approximation, (c) parameters characterizing roughness.

and is approximated by the superposition of two piecewise-periodic functions, Fig. 7(b). Periodic fragments of the approximated function are described by sinusoids:

$$K_n = \frac{A_1^n}{A}\sin\left(\pi\frac{x_1^n-\ell_1}{\ell_1}\right)+\frac{A_2^n}{A}\sin\left(\pi\frac{x_2^n-\ell_2}{\ell_2}\right),$$
$$x_1^n = x_1^{n-1}+V_\tau^n\Delta t,$$
$$x_2^n = x_2^{n-1}+V_\tau^n\Delta t. \tag{20}$$

Here n is the number of a time step while $A_{1(2)}$ and $\ell_{1(2)}$ are the amplitude and half-period of a sinusoid, respectively. The current value of the coordinate axis x is directed along the contact surface line (tangential direction). The indices 1 and 2 indicate the number of a sinusoid while A is the size of a representative mesovolume.

The first sinusoid (number 1) in Eq. (20) is considered as the first approximation of the real dependence $K_\mu(\xi)$. The second sinusoid (marked 2) is approximation of the real profile, Fig. 7(b). Each sinusoidal component of the complex curve $K_\mu(\xi)$ has its own eigenvalue of the amplitude A_0 which correlates with the average values of amplitudes given for the first and second sinusoids $A_{1(2)}^{\text{aver}}$ (Fig. 2.7(c)).

To estimate the characteristic length of the curve $K_\mu(\xi)$, the parameters d_1 and d_2 are introduced, Fig. 7(c). Each periodic (sinusoidal) portion of the curve has its own length, that correlates with the average value of $d_{1(2)}$ and those for $A_{1(2)}^{\max}$ and $\ell_{1(2)}$. They can be obtained from experiments and/or theory using the models in [22,23,25].

In general, the curve $K_\mu(x)$ oscillates about some average value of K_μ^{av}, greater than zero. This value is independent of F_{N} and can be determined only by the contact profile of the surfaces. The condition $K_\mu^{\text{av}} > 0$ is governed by the surface characteristics such as pits, etc.

And quantified by the characteristic length R at the mesolevel. The interaction of two bumps at the microlevel of the "stick–slip" mechanism and $K_\mu^{\text{av}} = 0$. With two cellular automata interacting at the mesolevel, irrespective of the interaction of the basic mechanisms there always exists some surfaces such that $K_\mu^{\min} > 0$. Note that the oscillation amplitude K_μ decreases to zero with increasing R.

2.7. Energy dissipation

Eqs. (6) and (7) describe the systems behavior for constant total mechanical energy. To include energy dissipation, for instance heat generation consider Lagrange function of the automata ensemble that depends on the generalized coordinates q and generalized velocities $\dot{q}$ as

$$L = K - U,$$

where $K = K(\dot{q})$ is kinetic energy and $U = U(q)$ is potential energy. The equation of motion is

$$\frac{\mathrm{d}}{\mathrm{d}t}\left(\frac{\partial L}{\partial \dot{q}}\right) - \frac{\partial L}{\partial q} + \frac{\partial D}{\partial \dot{q}} = 0, \tag{21}$$

where the dot denotes time differentiation, $D = D(\dot{q})$ is additional function depending on generalized velocities only; it accounts for dissipation. Introduce the temperature T as

$$C_v m\dot{T} = \frac{\partial D}{\partial \dot{q}}\dot{q},$$

where C_v is specific heat capacity and m is the automaton mass. Eq. (21) the result is

$$\dot{L} = \frac{\partial L}{\partial \dot{q}}\ddot{q} + \left[\frac{\mathrm{d}}{\mathrm{d}t}\left(\frac{\partial L}{\partial \dot{q}}\right) + \frac{\partial D}{\partial \dot{q}}\right]\dot{q}.$$

It is possible to show that the equations of motion can be written as

$$\left[L - \frac{\partial L}{\partial \dot{q}}\dot{q} - C_V m T\right]^{\bullet} = 0$$

or

$$[K + U + C_V m T]^{\bullet} = 0. \tag{22}$$

It follows from Eq. (22) that the expression in brackets represents the total energy with dissipation that is constant in time.

3. Transient to steady-state deformation

3.1. Problem description

Material has been studied either during steady mode of deformation or at the onset of fracture [26,27]. Material behavior at the initial stages of deformation remain has not much attention. Experimental study of the problem is possible only by total deformation, acousto-emission spectra, etc. Even in this case, higher time precision in the range 10^{-6}–10^{-9} s measurement equipment is necessary. Spatial distribution of deformation may be obtained with high accuracy using the special television-optics system [28,29]. Displacement vectors can be assessed on the surface of the deformed material with the accuracy of 1500 points per 1 mm^2. With high time resolution details of transition to stationary deformation mode at the mesolevel can be found. Discrete approaches [12,30–36] are also being widely used in deformation studies. In what follows, the method of MCA [32–36] will be applied to obtain the response of solids at the transition stage when the material deformation occurs already.

3.2. Modeling consideration

A 2D sample is simulated to study the material response at the mesolevel under load. The structure of the sample is shown in Fig. 8(a). The automata are taken to be pure Ni or Al [37].

Considered are uniaxial tension and compression with the constant rate V_Y. The load is applied to the bottom part of the sample. Calculations are made for three different loading rates $V_Y = -10$ cm/s; $V_Y = -1$ cm/s and $V_Y = -0.1$ cm/s.

It was shown in [34], that the tension of Ni samples reached the steady-state of deformation when $t = 5$ μs. The flat steady-state deformation begins to propagate at $t = 0.05$ μs. Evolution of velocity field shows the region of compressive stresses follows the front along the material surface. The size of this region is about 30 μm along the OY axis, Fig. 8(b) for an automaton of size 4 μm. This compression region propagates immediately after the wave front reaches the steady-state of deformation. This region is not affected by surface defects. That inner structure of the velocity distribution, however, is affected by surface defect. Such features are expected to be observed from the acousto-emission spectra.

Additional work in [34] shows that such regions present in compression were attributed to the

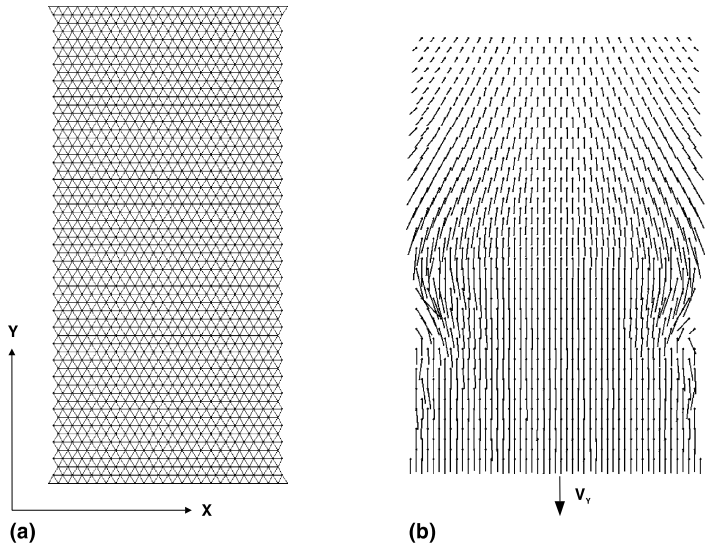

Fig. 8. Linked automata (4 μm) connected with lines for specimen $X = 0.1$ mm, and $Y = 0.2$ mm: (a) sample structure, (b) velocity field at $t = 0.26$ μm and $V_Y = 10$ cm/s.

tendency of the material to keep its initial volume. Such regions also arise in surface layer where the material is free to move in direction normal to applied loading. For periodic boundary conditions on the lateral boundary of the sample, compressive regions were not detected. Once the compression region is generated, it propagates along the surface with the velocity of transversal acoustic wave. It propagates into the bulk of the material with the speed of longitudinal acoustic wave. Calculations have shown that the compression regions propagate into the material from two opposite sides of the material. They interfere and destroy each other. For hardened surface where the elastic moduli of the surface automata are increased by 2–4 times, the speed of propagation of the compression region along the surface was found to be increased by 10–15%.

In reality, the loading may not be oriented along the sample axis. Shear stress may prevail. It is therefore relevant to study aluminum samples subjected to tension + shear with $V_X = 12.5$ m/s and $VY = 3.75$ m/s, compression + shear with $V_X = 12.5$ m/s and $V_Y = -3.75$ m/s is also considered. The structure of the sample is shown in Fig. 8(a). The size of each automaton was 3 μm.

Preliminary MCA calculations show that for the combination of shear loading and free surface steady "vortex" associated with elastic deformations move with a velocity determined by the transverse acoustic wave. Distribution of elastic deformation during the transitory period before it becomes steady is highly non-uniform [35]. Fig. 9(a) shows the velocity field and a schematic distribution of directions of elastic displacements. Fig. 9(b) exhibits the initial formation of "vortex". This is caused by the influence of free surface as in the case of tensile load. The surface properties influence the shape of the "vortex" that depends on its generation and propagation features. For a hardened surface the vortex is more localized and tends to be formed deeper into the material. Deeper vortex generation corresponds to wider samples. The generation of vortex appears to be associated with the interaction of two compression regions one of which propagates from the loaded surface and the other is reflected by lateral surface of the sample.

To reiterate, the simulated deformation under tension is also of the vortex type caused by the free surface. The "vortex" is formed on the opposite side of the sample as compared to compression. For a long sample the vortex at the

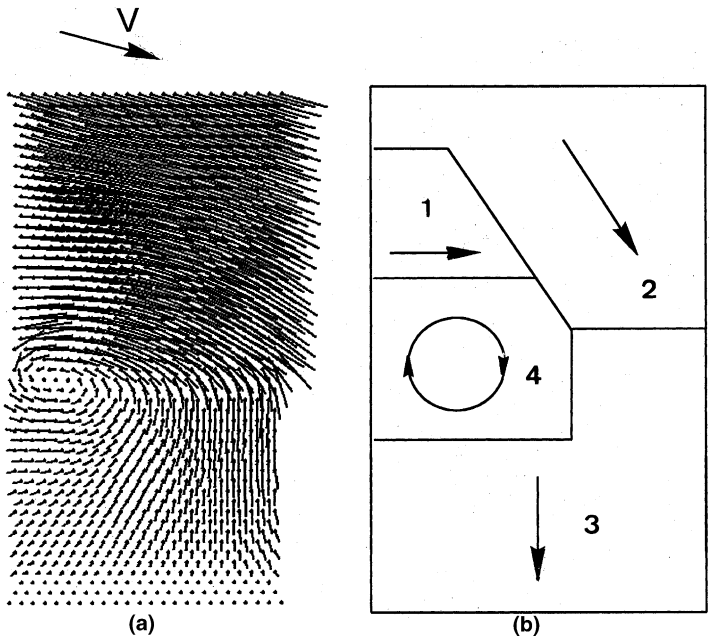

Fig. 9. Combined shear loading and free surface steady vertex: (a) velocity field at $t = 0.022$ μs (compression + shear), (b) direction of elastic displacements.

opposite side of the sample has an opposite rotation. The process of new vortex generation can be divided into four stages. At the first stage, it is possible to define a wide enough band of uniform displacements with shear component Figs. 10(a) and (b). The band is located ahead of the vortex. The second stage pertains to the core of a new vortex in Fig. 10(c) that appears lower than the displacement band at the lateral surface. It is opposite to the shear component direction. At the third stage, this new vortex grows and departs from the initial vortex, Fig. 10(d). At the fourth stage, the sizes and velocities of the new and initial vortices are equalized. The distance between the vortices is determined by the size of the sample and its elastic properties. Thus the transient to steady mode of deformation in long samples may be identified by wavy displacement field.

Thus, according to the obtained results, the stressed state of the material is essentially non-uniform even at the stage of transient to steady mode of deformation.

4. Computer aided design of concrete material and structures

4.1. Preliminary remarks

Concrete is a highly heterogeneous material. Its response can change dramatically with load type. For instance, structures that may be safe under normal conditions can be destroyed by a relatively insignificant movement of the soil during an earthquake.

The MCA approach will be applied:

- to study the fracture process of concrete specimens and structures,
- to develop computer-aided design procedures for concrete members and constructions,
- to propose an architecture of an intellectual electronic dynamic monitoring system for acquisition, storage, communication and data processing of full-scale experiments on fracture of real structures and show the possibility of applying the MCA method to predict vulnerability of structures.

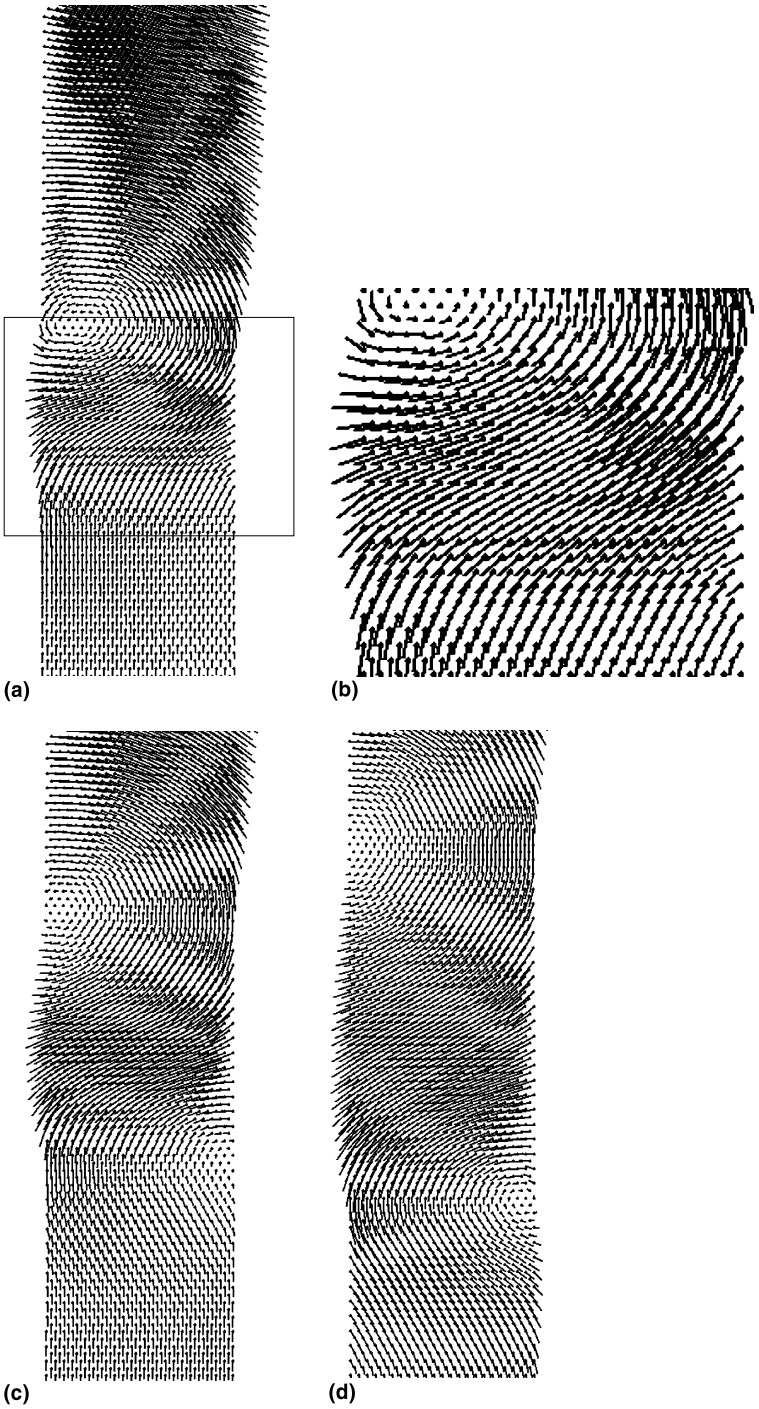

Fig. 10. Velocity field for a long sample at different time: (a) $t = 0.065$ μs, (b) enlarged section of (a), (c) $t = 0.095$ μs, (d) $t = 0.165$ μs.

4.2. Concrete specimen

Cement paste and aggregates are the main constituents of concrete. The strength of concrete depends on their properties and curing conditions. According to the MCA method, the inner structure of concrete specimens can be represented by two types of automata. First automata consist of the properties of cement paste and second with properties of aggregates. The MCA computer-aided design of concrete can be made following the scheme:

Step 1: Uniaxial compression test of cement and aggregates are made. The results are presented in terms of the stress–strain diagrams as shown in Fig. 11. Note that the MCA simulation fits the data well.

Step 2: Consider a concrete specimen 15 cm in the OX direction and 30 cm in the OY direction. The inner structure of the specimen is generated by "computer-aided mixing" of the aggregate and cement paste automata. The resulting concrete specimen is shown in Fig. 12. Concentration of aggregate-automata is about 52%.

Step 3: The computer simulated concrete specimen is subjected to uniaxial loading with a constant rate. The stress–strain diagrams of experimental test [38] and MCA simulation are shown in Fig. 13. Note that the obtained results are very close to experimental data.

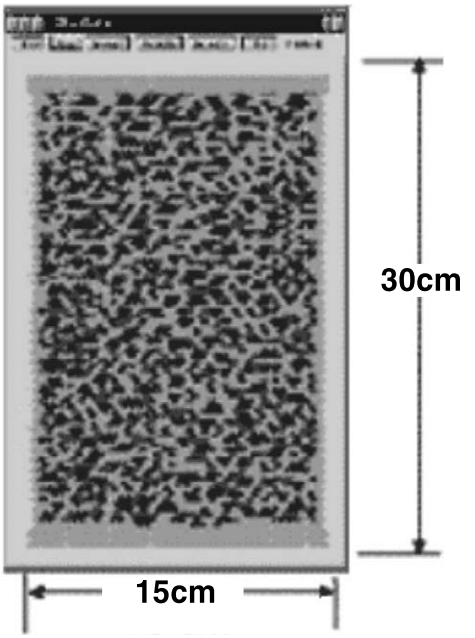

Fig. 12. Concrete specimen.

Modeling results based on MCA, show good agreement with experimental data for strength properties and fracture patterns [38].

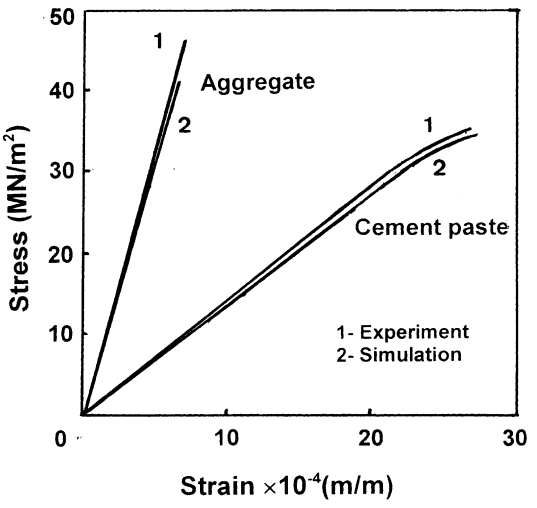

Fig. 11. Stress–strain diagrams for cement paste and aggregate.

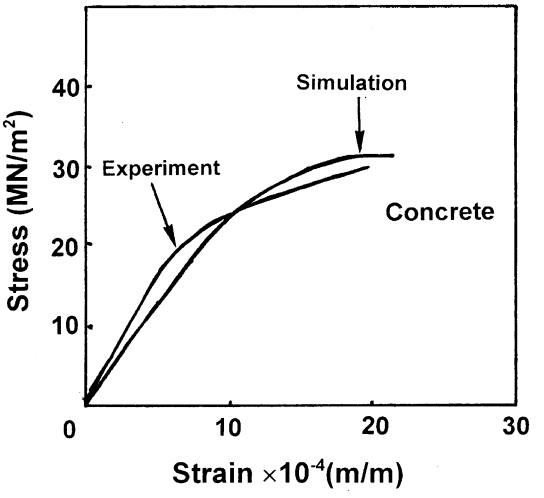

Fig. 13. Stress–strain diagrams of experimental test and MCA simulation.

4.3. Dynamic tests of structures

Consider the fracture behavior of a two-story frame under shear-type deformation imitating earth crust movement during an earthquake.

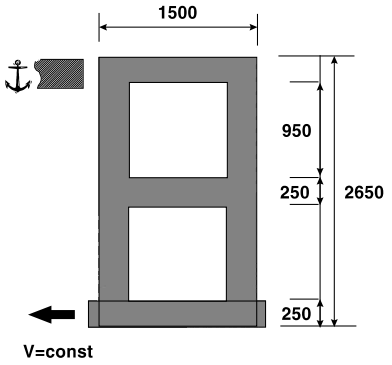

Fig. 14. Loading scheme of the sample (all units in cm).

Fig. 14 shows the loading scheme. Fig. 14 shows that the stationary stopper limits the movement of the "roof". Bottom of the structure models the foundation lying on the earth and shifted with it during an earthquake. A separate automaton of the structure was considered as the concrete. The mechanical properties of an automaton coincide with those found previously using MCA CAD.

Specific characteristics of cellular automata and parameters of inter-element interaction were measured using the parameters of high-strength concrete. Damping of the upper floor of the structure with a stationary stopper (Fig. 14) controls the bending type of structure deformation. Fig. 15(a) shows the primary of the fracture patterns under the above mentioned loading conditions. Fig. 15(b) shows the prime stages of structure fracture for the thickened middle beam. Note that cracks are first initiated and grow near the butt-joints where the middle beam is connected

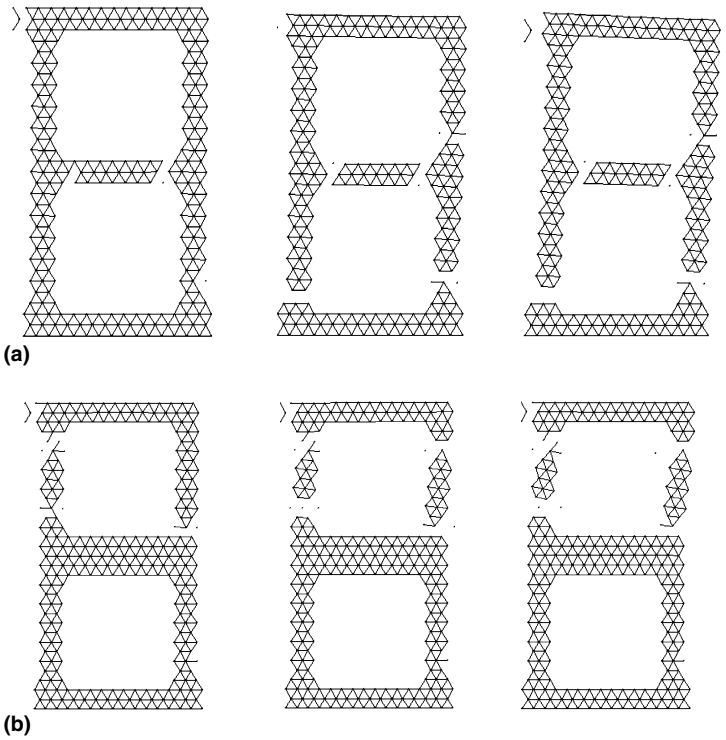

Fig. 15. Structure of inter-element bonds at different stages of fracture: (a) primary fracture patterns, (b) fracture patterns for thickened mid section.

to the walls of the structure. The MCA method makes it possible to analyze the design modifications of the frame in order to delay structure fracture.

4.4. Intelligent expert systems for viability analysis of structures

To design an acquisition system for measuring, storing and monitoring the displacements of selected points on an object undergoing dynamic loading, a high rate of network data exchange among the nodes is needed.

The MCA method requires each module to be capable of executing at least 10 K measurements per second within a large range of acceleration values. Furthermore, it should contain acceleration sensors capable of measuring in 3D and storage capacity of the order of 100 K values within a few seconds. Hence, the sensor modules should be robust enough to withstand and survive the impact of building collapse. That is the monitoring connections should be intact so that the crash data can be extracted from the module for subsequent analysis using the MCA system. Depending on the type of crash data needed, the acquisition system may require several hundred modules.

Acceleration sensor technologies have improved (primarily with reference to monitoring crash data). However, their application is complex. As shown in the block diagram of the sensor module designed (Fig. 16), an array of sensors are analog multiplexed to an A/D converter that feeds a FIFO RAM with sample values under control of range-dependent sensor selection logic. Even more difficult is the power supply and synchronization, that is synchronization of samples in separate modules. The high sampling frequency and the possible breakdown of network connection will require more advanced design considerations to assume reliable operation under high-G conditions. Accuracy and safety features should be implemented in the module such that response of order of several microseconds could be maintained for about ten seconds after the loss of external synchronization due to wire disconnection.

The sensory modules are attached to the network as shown in Fig. 17. The network controller is located at a safe remote place away from the crash site. Two types of network architecture are need for sensor modules with reference to their data storage and transmission capabilities. The first pertains to local data storage and slow transmission to the host system after termination failure. The second consists of modules from

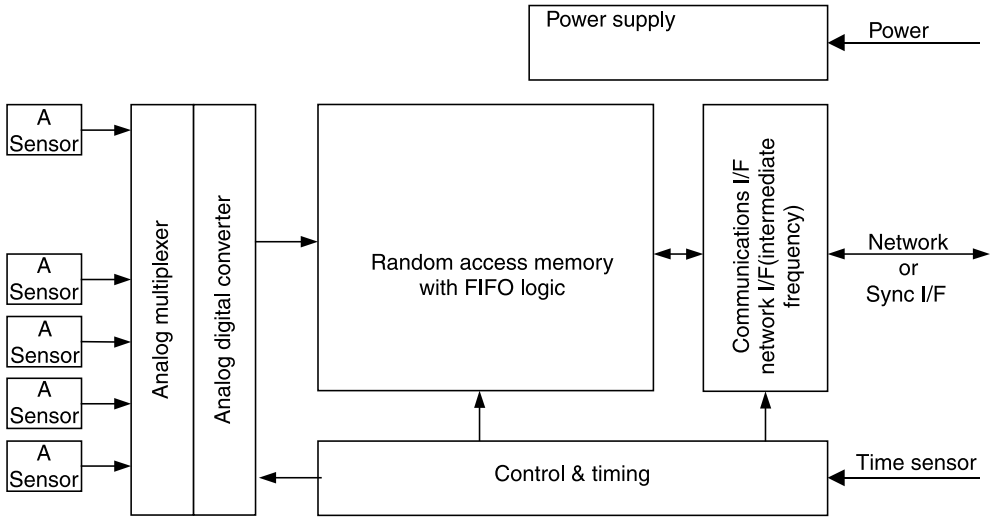

Fig. 16. Flow chart of sensor module.

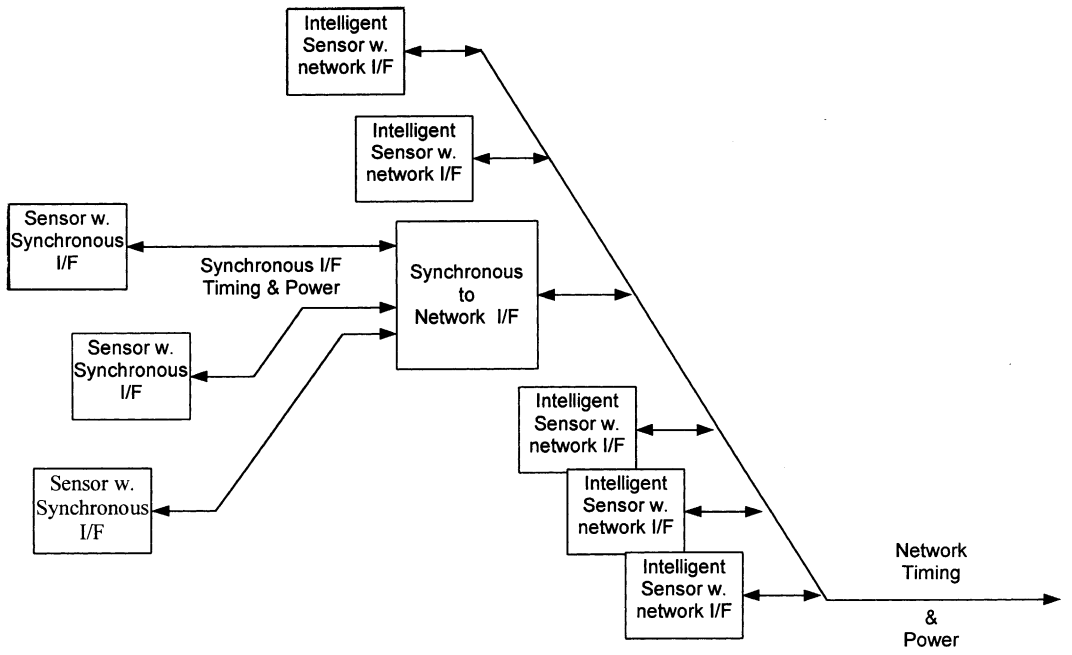

Fig. 17. Diagram of sensor-module connections.

which data are to be transmitted in real-time and minimizing the loss of communication due to possible sensor destruction. In view of the large number of sensor modules using a combined approach may be the best solution. For the case of microprocessor-based (including Neuron-based) intelligent modules, generation and transmission of alarm events based on thresholds of acceleration values could be implemented. Another technology is digital signal processing for efficient compression and buffering of data recorded.

Coarse values of acceleration can be transmitted during execution of the crash test in real-time to support the planned real-time functions of the MCA system. Note that most of the data collected during execution of the test will be stored locally and will be subsequently transmitted through the network to the MCA system for further analysis. This makes it possible to combine the MCA method and the sensor system suggested above into one intellectual integrated system. The resulting system allows one not only to carry out monitoring of structures and constructions but also to expert their vulnerability under different loading conditions.

5. Computer aided examination of strength properties of lignite

5.1. Statement of problem

Danger of mine roof and wall collapse is an important problem for coal mining [39]. For examination of the collapse hazard of coal-beds and for design of protective structures, knowledge about strength properties and fracture features of coal is extremely important. Lignite is a strongly marked heterogeneous material. Therefore, elastic characteristics, strength properties as well as mechanisms of lignite fracture can be changed dramatically even under small changing of its composition or loading conditions.

For safety of coal mining, forecasting of tunnel roof and wall collapse is one of utmost importance. The sudden outbursts of coal and gas could lead to collapse and delay construction of the mine

roadways of the uncaved portion. The Velenje coal mine (one of the biggest mines in Europe) there has experienced 7 such accidents with 11 dead miners since 1958.

Experimental procedure for investigation of the strength properties and load carrying capacity of lignite can be obtained from standard tests. This includes compression, tension, shear tests, etc. These data, however, are not enough to predict failure of materials under real conditions, because lignite behavior depends sensitively on load conditions. In the coal-beds lignite is under severe compression. But lignite near the surface of the tunnel in the coal-bed is under very complex loadings. It is very difficult and often impossible to reproduce these conditions in the laboratory. Moreover, the mechanical properties of lignite depend strongly on its microstructure being inhomogeneous [40]. Similar specimens from the same bore-hole with a given microstructure are impossible to simulate for the various different loads.

Computer-aided simulation could reproduce the original conditions of lignite bedding and predict its mechanical properties under real conditions of coal beds. Moreover, it can reproduce conditions in the coal beds after laying the tunnels or other mining activities as well as during earthquake. The MCA method will be applied to investigate the response and fracture process of lignite specimens under mechanical loads of various types.

5.2. Simulation

Lignite can be described macroscopically in terms of lithotypes and microscopically in terms of macerals [41]. The basic four lignite lithotypes are known as: detritic, xylitic, fusinitic and mineral-rich lignite. Lignite composition is treated as an indirectly important factor for potential coals and gas outbursts, especially fine detritus. An internationally accepted classification for lignite lithotypes still does not exist. In the case of Velenje coal mine, an adapted lithotype system for the Velenje lignite was developed, Table 1.

Detritic lignite (Category VI) is composed of very fine detritical particles. For mineral matter admixtures, it can contain up to 10% of xylitic fragments. If the xylitic content is greater than 10%, the lithotype is termed as xylitic lignite (Categories I–V). Gelified lithotypes of lignite is described by Category VII. Macropetrographic logging of bore-holes, coal faces or samples have been made by estimating the corresponding volumes.

Table 1
Classification of lignite lithotypes (gD – rough detritus; dD – fractional detritus; Ks – xylite; g – gelite.)

Cagegory	Composition mark
I	100% Ks
II	<85% gD
III	<30% gD
IV	>85% dD
V	>90% dD
VI	100% dD
VII	>10% g

The aforementioned lignite categories have different elasto-plastic characteristics and strength, Fig. 18. At least 2 of them (Categories VI and VII) present a significant danger for mines. It should also be emphasized that coal fracture mechanism can change dramatically depending on its compositions.

5.3. Lignite fracture

Fracture of lignite under uniaxial compression loading is considered. Lignite cylinders of standard size were used for simulation by the MCA method.

Testing of lignite components. Lignite properties are obtained from computer simulation tests in compression for xylite, detritus and gelite. The basic model parameters of automata for each components of lignite were fitted. These parameters are elastic limit, strength, strength strain and so on.

Fig. 19(a) gives a comparison of the stress–strain diagrams. Note that xylite has a fibrous structure. Hence, mechanical properties of xylite under compression depend on rational fibres orientation. This dependence is exhibited in Fig. 19(b) for fiber orientations of 0°, 40° and 90°.

Fig. 19(a) shows that xylite is highly nonlinear in the stress versus strain response. For detritus,

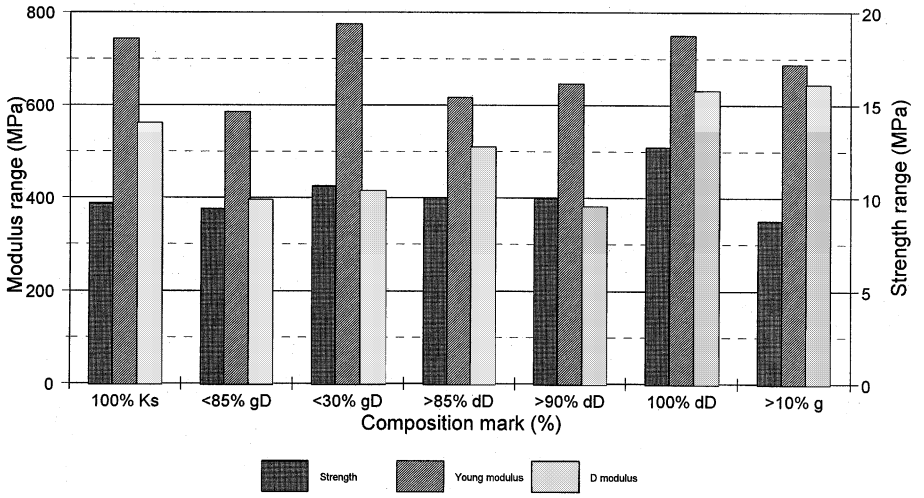

Fig. 18. Mechanical properties of lithotypes.

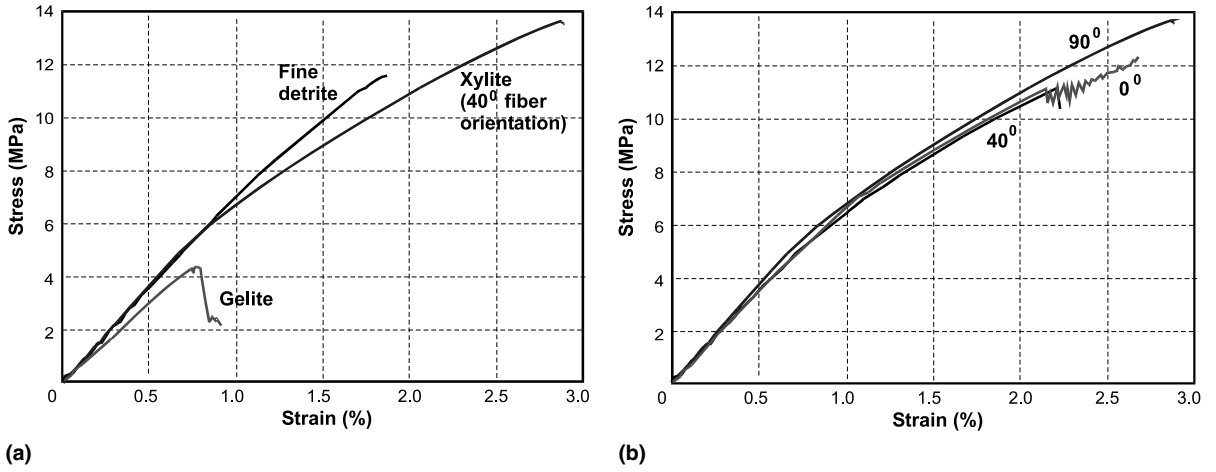

Fig. 19. Stress–strain diagrams of lignite and xylite: (a) lignite components, (b) xylite with various fibres orientations.

stress–strain profile is closer to linear. Gelite exhibits highly brittle behavior.

While the xylite stress–strain diagrams for different fibre orientations are close but the corresponding fracture patterns can be quite different. This can be seen from Fig. 20(a)–(c) where the results of compression test of cubic specimens of xylite with fiber orientations of 90°, 0° and 40° with respect to the load direction. For vertical fibers the cracks propagated in the direction of fibers. When the fibers are aligned horizontally, multiple breaks occurred between fibers but there are no long horizontal cracks. This is because initial damages tend to grow in the horizontal direction but the specimen geometry and loading favors another direction of crack propagation. This leads to a very complex fracture pattern. When the fiber orientation is 40°, the fracture pattern contains features of the two previous examples.

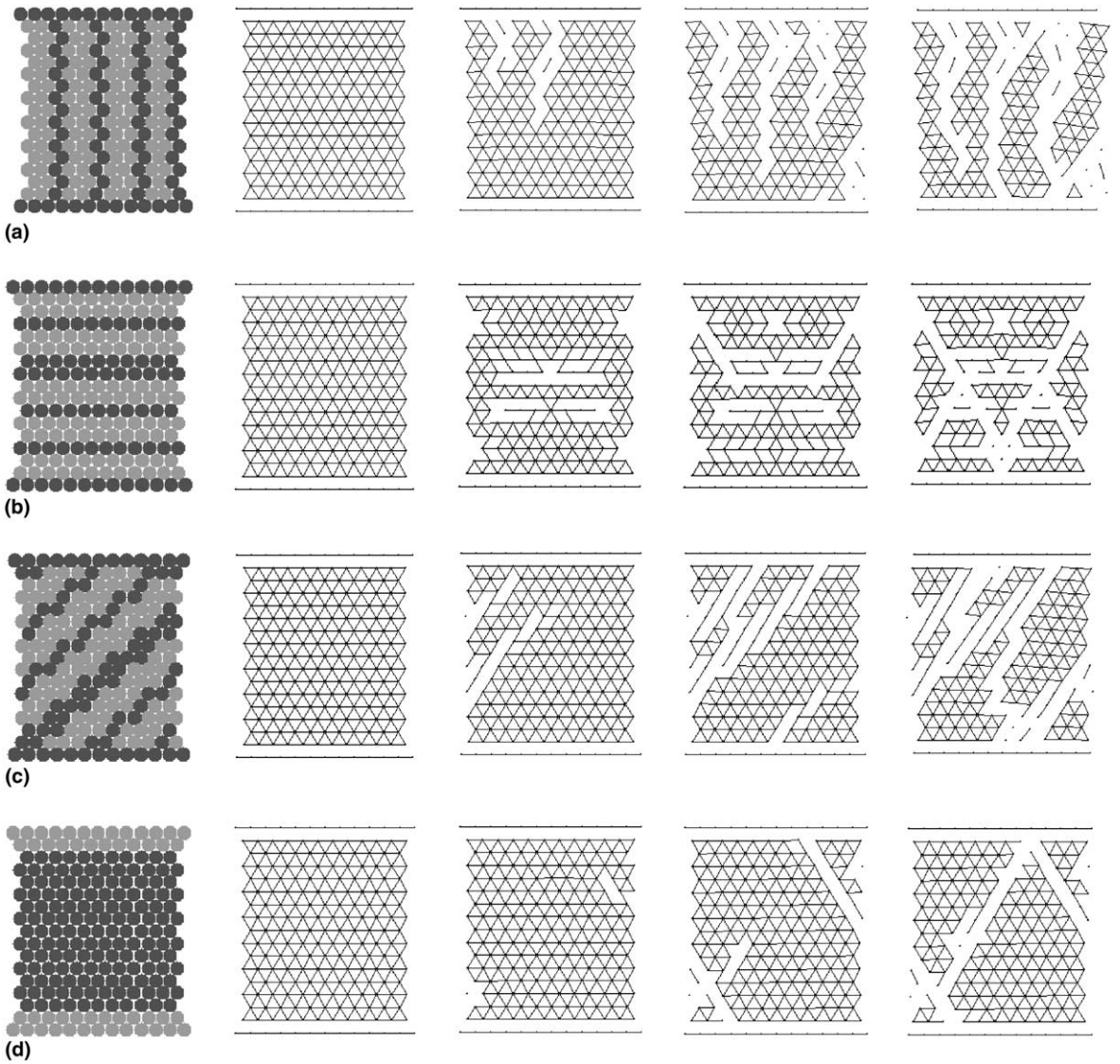

Fig. 20. Structure and evolution of inter-automata bonds under load: (a) xylite 90° orientation, (b) xylite 0° orientation, (c) xylite 40° orientation, (d) fine detritus.

For comparison, the fracture evolution of detritus specimen is presented in Fig. 20(d). This lignite component is not oriented. Hence, the direction of crack propagation is dictated by the specimen geometry and loading. The structure of gelite is partially oriented.

Testing of lignite specimens: After fitting the parameters associated with the compression test of lignite specimens, various categories can be identified. Computer simulation tests have been made for three different categories of lignite in accordance with the Velenje coal mine classification. They are:

- Category II (<85% xylite).
- Category IV (>15% xylite).
- Category VI (<20% gelite).

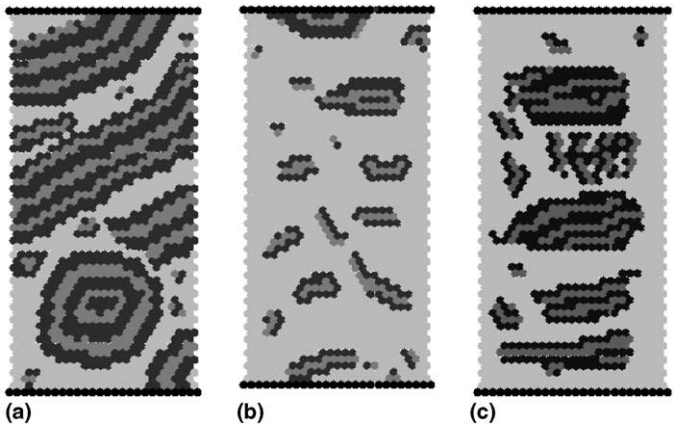

Fig. 21. Structures of lignite specimens: (a) Category II, (b) Category IV, (c) Category VI .

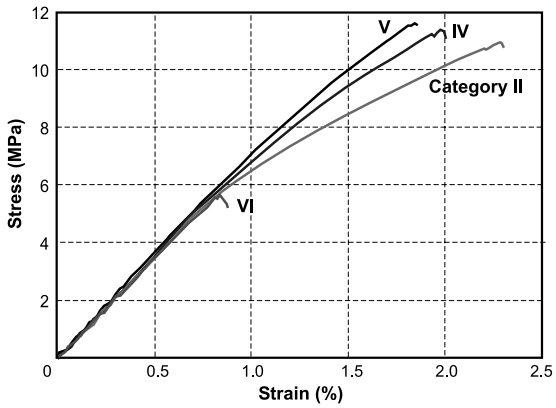

Fig. 22. Stress–strain diagrams of four tested lignite specimens.

Structures and size of the specimens are shown in Fig. 21. In Fig. 22 comparison is made for the stress–strain diagrams for Categories II, IV, V and VI.

Fig. 22 shows that the linear and nonlinear (degradation) parts of the curve depend on the lignite composition. Response characteristics of lignite of Category II are very close to those of xylite. Decreasing the xylite part leads to increasing the proportion of linear and nonlinear parts of the curve. In case of pure detritus, the specimen response is brittle and fracture has an explosive feature. The presence of gelite decreases the strength considerably and limits the ultimate strain of lignite. These simulated results are in good agreement with experimental data.

Fig. 23 show evolution of simulated specimens under applied compressive load. Though the specimen geometry and the loading tend to dictate the directions of damage, material microstructure also plays a role. Fig. 23(a) shows that cracks tend to grow along the fibers. The presence of xylite at the lower part of the specimen leads to crack propagation around the xylitic fragment. Fig. 23(b) shows diagonal propagation of the main crack. Gelified lignite damage is shown in Fig. 23(c) which initiates inside or on the surface of gelite fragments.

(a) Category II
(b) Category IV
(c) Category VI

Real compression test results for cylinder lignite specimens are shown in Fig. 24(a). Appearance of main diagonal crack that destroys the specimen can be seen. Before the main crack propagates a small piece of lignite at the lower left part is slivered from the specimen. This shown in Fig. 24(b).

The results of simulation show that lignite exhibits different types of fracture behavior that ranges from brittle to quasi-plastic. These results agree with experimental data. It shows that the MCA method can be applied to stimulate fracture behavior of heterogeneous media under standard test conditions and complex loading that is difficult to reproduce by experiments.

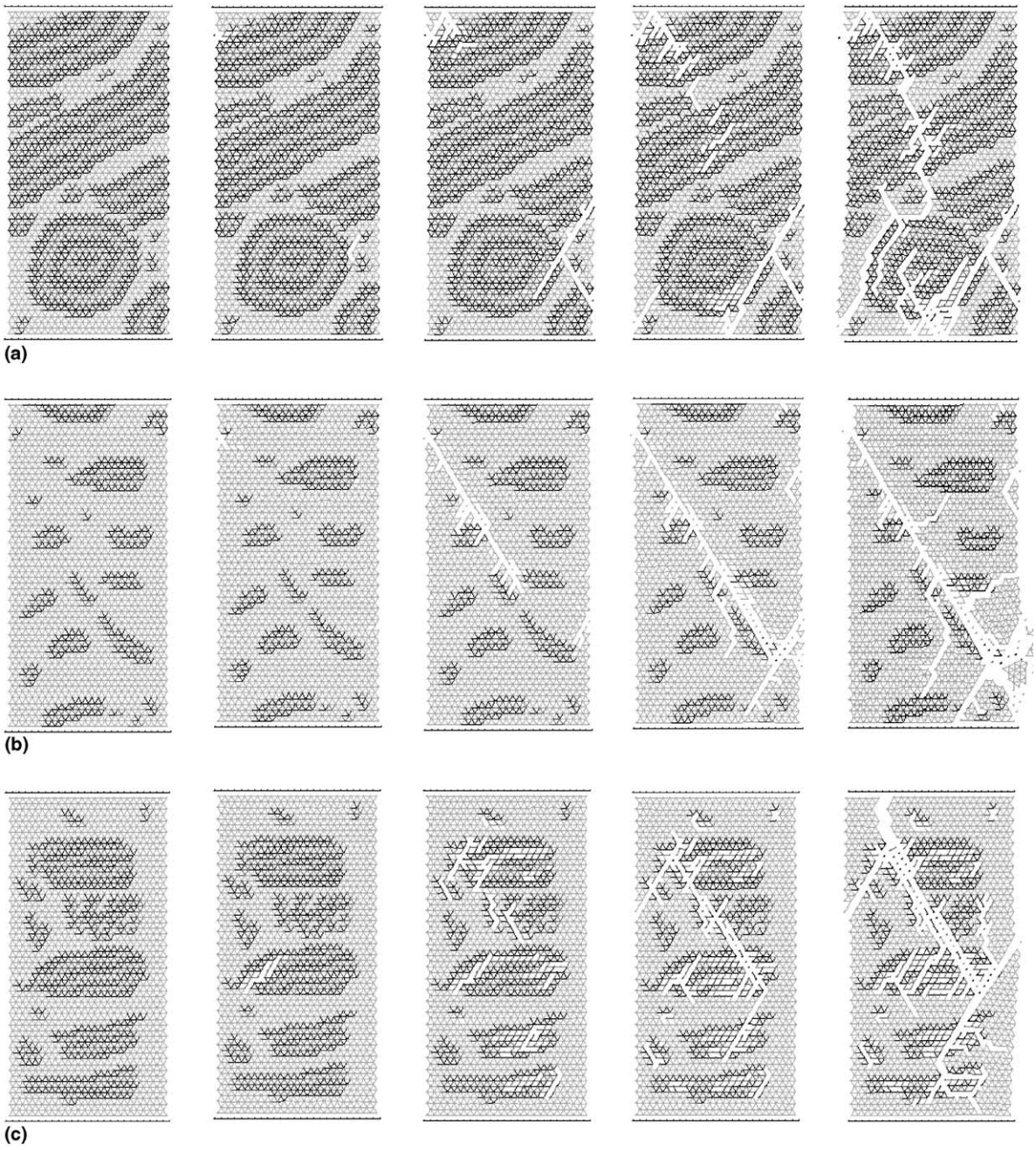

Fig. 23. Evolution of system of inter-automata bonds under loading for lignite specimens: (a) Category II, (b) Category IV, (c) Category VI.

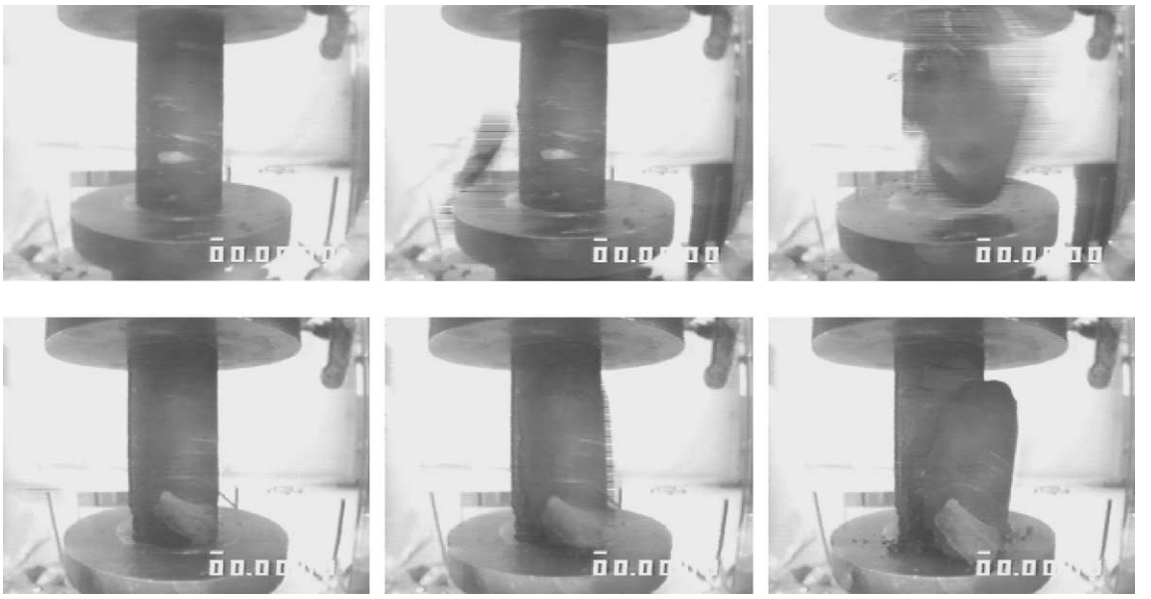

Fig. 24. Main stages of fracture of (a) real lignite specimens under uniaxial compression, (b) specimens fracture.

6. Fracture energy under dynamic loading

6.1. General remarks

Structural dynamics involves cars or transport vehicles under impact. The analysis entails the transformation of kinetic energy of interaction to the energy required to fracture at least a portion of the structure. Similar problems also exist in materials science where modern materials are heterogeneous and have a complex internal structure. To optimize a material structure for carrying dynamic load it is necessary to account for redistribution of elastic energy connected with phase transition, generation and accumulation of microdamages, etc for they influence the strength characteristics of the material [19,42–44]. These problems may be solved by the MCA method which has been successfully used for modeling fracture of the different materials [14,16,44–46].

Several problems of practical interest will be presented. In particular, the frame in Fig. 25(a)

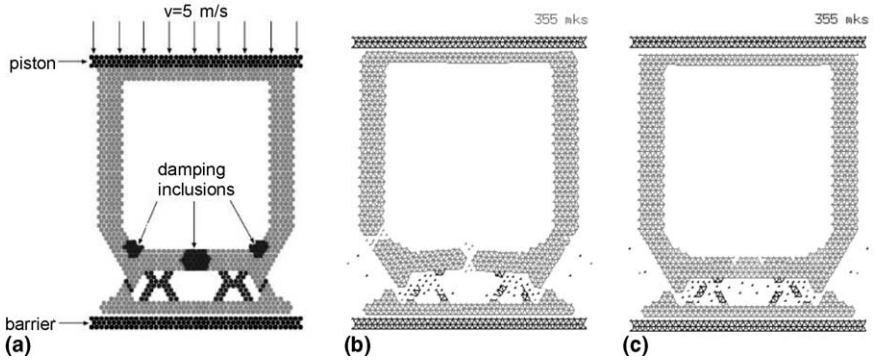

Fig. 25. Schematic of loading and fracture patterns: (a) fracture patterns of the modeled structures $t = 355$ μs, (b) frame without inclusion (base), (c) frame with inclusions.

will be analyzed. The objective is to alter the local damping by changing the stiffness such that energy would be more uniformly distributed. This would increase the load carrying capacity of the frame.

The load is applied a "piston" with velocity of 5 m/s, mechanical properties of the material correspond to those for ZrO_2 ceramics. They have been obtained by the MCA method [14,16]. The sample width is 4 cm, the height is 5 cm and the size of the automaton is 0.1 cm. The parameters of the automata correspond to those for concrete.

6.2. Fracture of structures

Numerical experiments of "collision" show that the center and the corners behind the front wall of the modeled structure undergo maximal local deformation. Fig. 25(b) shows the damage pattern. Hence, additional damping was added to these regions. This is accomplished by a reduction of the Young modulus by a factor of 2 when compared with the base structure material. The load carrying capacity of the structure is thus improved, and the damage is considerably less. Fig. 25(c) also shows a linkage structure with additional damping at the same time $t = 355$ μs as in Fig. 25(b). By softening the local regions of the structure larger local displacements would result. This would reduce the stress concentration effects by a more uniform distribution of elastic energy. This would effectively raise the threshold of the energy absorbed by the structure before losing its carrying capacity.

7. Conclusion

This work has provided a description of the method of MCA and results for a limited number of applications. The method will be further expanded to cover a wide range of problems [47,48]. In particular it can treat problems at the mesolevel with explicit account of the anisotropy of representative volumes and at the macrolevel where approximate isotropy of the automata response could be assumed depending on the response function of a cellular automaton. One of the advantages of this approach is the direct simulation of the fracture process. Additional features of the MCA method can be developed. Change of the shape of automata is being considered. This would provide a wider range of plastic deformation simulation. 3D MCA is being developed in addition to fluids, chemical reactions, etc.

References

[1] P.A. Cundall, O.D.L. Strack, A discrete numerical model for granular assemblies, Geotechnique 29 (1) (1979) 47.
[2] P.A. Cundall, A computer simulations of dense sphere assembles, in: M. Satake, J.T. Jenkins (Eds.), Micromechanics of Granular Materials, Elsevier, Amsterdam, 1988, p. 113.
[3] H.J. Herrmann, Simulating granular media on the computer, in: P.L. Garrido, J. Marro (Eds.), 3rd Granada Lectures in Computational Physics, Springer, Heidelberg, 1995, p. 67.
[4] J. Hemmingsson, H.J. Hermann, S. Roux, On stress networks in granular media, J. Phys. I 7 (1997) 291.
[5] O.R. Walten, Numerical simulation of inclined chute flows of monodisperse, inelastic, frictional spheres, Mech. Mater. 16 (1993) 239.
[6] O.R. Walten, Numerical simulation of inelastic, frictional particle-particle integration, in: M.C. Roco (Ed.), Particulate Two-phase Flow, Butterworth–Heinemann, Boston, 1993, p. 884.
[7] S. Luding, Granular materials under vibration: Simulations of rotating spheres, Phys. Rev. E 52 (4) (1995) 4442.
[8] T. Poschel, Granular material flowing down an inclined chute: A molecular dynamic simulation, J. Phys. II 3 (1993) 27.
[9] D. Greenspan, Particle modeling in science and technology, Coll. Math. Societatis Janos Bolyai 50 (1988) 51.
[10] G.P. Ostermeyer, Many particle systems, in: German-Polish Workshop 1995, Polska Akad. Nauk, WarszawaIns. Podst. Prob. Techniki (1996).
[11] G.P. Ostermeyer, Mesoscopic particle method for description of thermomechanical and friction processes, Phys. Mesomech. 2 (6) (1999) 23.
[12] R.W. Hockney, J.W. Eastwood, Computer Simulation Using Particles, McGraw-Hill, New York, 1981.
[13] D. Potter, Computational Physics, Wiley, London, 1973.
[14] S.G. Psakhie, S.Yu. Korostelev, A.Yu. Smolin, A.I. Dmitriev, E.V. Shilko, D.D. Moiseyenko, E.M. Tatarintsev, S.V. Alexeev, Movable cellular automata method as a tool for physical mesomechanics of materials, Phys. Mesomech. 1 (1) (1998) 89.
[15] A.I. Dmitriev, S.Yu. Korostelev, G.P. Ostermeyer, S.G. Psakhie, A.Yu. Smolin, E.V. Shilko, Movable cellular automata method as a tool for simulation at the mesolevel, Proc. RAS Mech. Solids 6 (1999) 87.
[16] S.G. Psakhie, Y. Horie, S.Yu. Korostelev, A.Yu. Smolin, A.I. Dmitriev, E.V. Shilko, Movable cellular automata

method as a tool for simulation within the framework of physical mesomechanics of materials, Rus. Phys. J. (11) (1995) 1157.
[17] Yu.M. Svirezhev, Nonlinear Waves, Dissipative Structures, and Ecological Catastrophes, Nauka, Moscow, 1987.
[18] S.M. Foiles, M.I. Baskes, M.S. Daw, Embeded-atom-method functions for the f.c.c. metals Cu, Ag, Au, Ni, Pd, Pt and their alloys, Phys. Rev. B 33 (12) (1986) 7983.
[19] V.E. Panin, Foundations of physical mesomechanics, Phys. Mesomech. 1 (1) (1998) 5.
[20] V.E. Panin (Ed.), Physical Mesomechanics of Heterogeneous Media and Computer-aided Design of Materials, Cambridge Interscience Publishing, Cambridge, 1998.
[21] S.G. Psakhie, D.D. Moiseyenko, A.Yu. Smolin, E.V. Shilko, A.I. Dmitriev, S.Yu. Korostelev, E.M. Tatarintsev, The features of fracture of heterogeneous materials and frame structures. Potentialities of MCA design, Comput. Mater. Sci. 16 (1999) 333.
[22] I.V. Kragelskii, Friction and Wear, Mashgiz, Moscow, 1962.
[23] W.W. Tworzydlo, W. Cecot, J.T. Oden, C.H. Yew, Computational micro- and macroscopic models of contact and friction: formulation, approach, and applications, Wear 220 (1999) 113.
[24] M.G. Rozman, M. Urbakh, J. Klafter, Stick-slip dynamics of interfacial friction, Physica A 249 (1998) 184.
[25] F. Raharijaona, X. Roizard, J. Stebut, Usuage of D roughness parameters adapted to the experimental simulation of sheet-tool contact during a drawing operation, Tribol. Int. 32 (1999) 59.
[26] A.F. Pimenov (Ed.), Plastic Deformation of Construction Materials, Nauka, Moskow, 1988 (in Russian).
[27] J.F. Bell, Encyclopedia of Physics. Vol. VIa/1. Mechanics of Solids I, Springer, Berlin, 1973.
[28] V.I. Syryamkin, V.Ye. Panin, Ye.Ye. Dyeryugin, A.V. Parfenev, G.V. Nerush, S.V. Panin, in: Physical Mesomechanics and Computer-aided Design of Materials, vol. 1, Nauka, Novosibirsk, 1995, p. 176 (in Russian).
[29] V.Ye. Panin, Methodology of Physical Mesomechanics as the basis for model construction of computer-aided design of materials, Rus. Phys. J. (11) (1995) 5.
[30] S. Walfram, Theory and Application of Cellular Automata, World Scientific, Singapore, 1986.
[31] G. Philippou, H. Kim, R. Rajagopalan, Comput. Mater. Sci. 4 (2) (1995) 181.
[32] V.Ye. Panin, V.A. Klimyonov, S.G. Psakhie, O.A. Atamanov, V.P. Bezborodov, V.V. Guzeev, S.P. Efimenko, A.A. Zabolotskii, E.E. Kovalevskii, S.Yu. Korostelev, Advanced Materials and Technologies. Design of Advanced Materials and Hardening Processes, Nauka, Novosibirsk, 1993 (in Russian).
[33] S.G. Psakhie, S.I. Negreskul, K.P. Zolnikov, S.Yu. Korostelev, A.V. Astapenko, E.V. Shil'ko, A.I. Dmitriev, S.V. Alekseev, D.Yu. Saraev, A.E. Kushnirenko, in: Physical Mesomechanics of Heterogeneous Media and Computer-aided Design of Materials, Cambridge Interscience Publishing, Cambridge, 1998.
[34] S.G. Psakhie, A.Yu. Smolin, S.Yu. Korostelev, A.I. Dmitriev, E.V. Shil'ko, S.V. Alekseev, Pis'ma Zh. Tech. Phys. 21 (20) (1995) 72 (in Russian).
[35] S.G. Psakhie, Ye.V. Shil'ko, A.I. Dmitriev, S.Yu. Korostelev, A.Yu. Smolin, Pis'ma Zh. Tech. Phys. 22 (2) (1996) 90 (in Russian).
[36] S.G. Psakhie, Y. Horie, S.Yu. Korostelev, A.Yu. Smolin, A.I. Dmitriev, E.V. Shil'ko, S.V. Alekseev, Movable cellular automata method as a new technique to simulate powder metallurgy materials, in: Proceedings of the International Conference on Deformation and Fracture in Structural PM Materials, Stara Lesna, Slovakia, 1996, pp. 210–220.
[37] I.S. Grigoriev, Ye.Z. Meilikhov (Eds.), Physical Values. Handbook, Entergoatomizdat, Moscow, 1991 (in Russian).
[38] A.M. Neville, Properties of Concrete, Wiley, New York, 1973.
[39] S. Zavshek, Dangerous occurences in the Velenje pit, in: Materials of 22nd Meeting of Miners, Izlake, Slovenia, 1997.
[40] M. Markich, R.F. Sachsenhofer, Petrografic composition and decompositional environments of the pliocene Velenje lignite seam, Int. J. Coal Geol. (11) (1997) 229–254.
[41] M. Markich, S. Zavshek, Lithotype characterization of the Velenje lignite. A short working issue, Velenje, Slovenia, 1999.
[42] E. Haug, J. Clinckemaillie, X. Ni, A.K. Pickett, T. Queckbarner, Recent trends and advances in crash simulation and design of vehicles, in: International Crashworthiness and Design Symposium ICD '95, University of Valenciennes, May 3–4, 1995.
[43] G. Lonsdale, J. Clinckemaillie, S. Vlachoutsis, J. Dubois, Communication requirements in parallel crashworthiness simulation, in: Lecture Notes in Computer Science, vol. 796, Springer, Berlin, 1994.
[44] S.G. Psakh'e, D.D. Moiseenko, A.I. Dmitriev, E.V. Shil'ko, S.Yu. Korostelev, A.Yu. Smolin, E.E. Deryugin, S.N. Kul'lkov, A possible method of computer-aided design of materials with a highly porous matrix, Tech. Phys. Lett. 24 (2) (1998) 154–156.
[45] S.G. Psakhie, E.V. Shilko, A.I. Dmitriev, S.Yu. Korostelev, A.Yu. Smolin, E.N. Korostelev, Self-organization effect in process of deformation of PM materials, Tech. Phys. Lett. 22 (12) (1996) 69–74.
[46] S.G. Psakhie, A.Yu. Smolin, E.V. Shilko, S.Yu. Korostelev, A.I. Dmitriev, S.V. Alekseev, About the features of transient to steady state deformation of solids, J. Mater. Sci. Technol. 13 (11) (1997) 69–72.
[47] S. Wolfram, Statistical mechanics of cellular automata, Rev. Mod. Phys. 55 (1983) 601–620.
[48] A.Yu. Loskutov, A.S. Mikhailov, Introduction to Synergetic, Nauka, Moscow, 1990.